Supplementary Information

The 28 January 2020, Mw7.8, Cayman Trough / Oriente Fault, Supershear Earthquake Rupture

longitude (degrees)	latitude	east	north	up (mm)	σ_{east}	σ_{north}	σ_{up}	SITE
-79.758	19.738	-133.2	-29.6	-4.3	1.3	1.1	4.8	CBMD
-68.359	18.564	-0.6	0.3	-2.8	1.7	1.4	5.7	CN05
-70.656	18.790	0.2	1.0	-1.1	1.7	1.4	6.2	CN06
-76.749	18.005	12.8	-6.3	-1.4	1.2	1.0	4.4	CN12
-74.534	24.065	-3.5	-2.1	-0.3	2.0	1.7	7.3	CN13
-73.678	20.975	-1.6	0.2	-0.7	1.4	1.2	4.9	CN14
-88.779	17.261	-0.2	0.9	-0.5	2.3	1.8	8.9	CN23
-69.940	19.667	-1.1	-0.3	-3.0	1.6	1.4	5.9	CN27
-81.363	13.376	0.3	2.1	-3.4	1.7	1.3	5.7	CN35
-75.263	10.793	-2.3	0.8	-7.8	1.3	1.1	4.3	CN37
-72.254	21.783	-2.1	0.8	-0.0	1.5	1.3	5.3	CN53
-68.917	18.449	-2.4	0.3	-1.7	1.8	1.5	6.1	CRLR
-69.044	18.768	-0.0	0.9	-5.7	1.9	1.6	6.8	CRSE
-81.378	19.293	-52.5	28.8	-11.5	1.6	1.3	5.7	GCEA
-81.183	19.313	-60.3	16.2	-13.0	1.8	1.5	6.3	GCFS
-72.538	18.235	1.2	-0.3	0.6	1.5	1.2	5.1	JME2
-80.082	19.668	-152.9	67.4	-15.6	1.4	1.1	4.8	LCSB
-80.907	25.866	-0.3	2.2	-5.6	2.2	1.9	8.1	MTNT
-70.716	18.445	-0.8	1.0	-1.4	1.8	1.6	6.6	RDAZ
-70.328	18.277	0.6	-1.4	2.6	1.9	1.6	6.8	RDBA
-70.680	19.452	-1.0	1.0	3.2	1.9	1.6	6.8	RDF2
-68.718	18.598	0.0	0.7	2.2	1.7	1.4	5.8	RDHI
-69.547	19.307	-0.4	-0.3	-0.4	1.4	1.2	4.7	RDLT
-71.077	19.539	-1.2	-0.4	-4.6	1.8	1.5	6.3	RDMA
-71.639	19.849	0.8	0.3	-4.5	1.7	1.4	6.1	RDMC
-69.041	18.980	-0.2	0.8	0.4	1.8	1.5	6.3	RDMS
-71.421	18.501	-0.2	0.8	0.4	1.8	1.5	6.3	RDNE
-69.911	18.461	-0.4	-0.3	-1.7	1.2	1.1	4.0	RDSD
-70.246	19.286	0.4	0.6	3.6	1.6	1.3	5.5	RDSF
-71.227	18.820	0.5	0.6	-1.9	1.6	1.4	5.7	RDSJ
-81.716	12.581	1.0	2.6	-5.8	1.7	1.4	6.1	SAN0
-69.306	18.461	-0.2	-1.2	-1.0	1.8	1.4	6.2	SPED
-71.341	19.475	0.1	0.1	-4.9	2.0	1.7	7.5	SROD
-86.867	20.868	-3.2	2.8	-5.7	2.1	1.8	7.7	TGMX
-86.868	20.869	-3.3	2.4	-3.8	1.1	0.9	4.0	UNPM
-74.861	10.794	-0.4	0.1	2.2	2.1	1.7	7.3	VPOL
-80.319	25.825	-1.7	1.0	-2.5	1.9	1.8	7.5	ZMA1
-77.850	21.422	-10.1	-13.9	-0.9	1.5	1.3	5.4	CN16
-76.635	20.365	-3.3	-4.9	-0.6	1.4	1.1	4.9	BYMO
-76.979	20.968	-8.1	-7.9	-5.3	1.5	1.3	5.6	LTUN
-82.803	21.892	-7.8	4.4	-8.2	1.8	1.5	6.9	ISLA
-81.210	23.029	-3.0	2.4	1.7	1.8	1.6	6.9	CARD

-82.395	23.121	-2.9	3.2	-5.0	2.0	1.8	7.4	HAVA
-77.409	19.914	0.5	-13.5	10.3	1.1	2.6	28.1	gpil
-75.902	20.369	-1.9	-5.4	-18.9	8.5	3.0	34.8	gmel
-75.906	20.005	-2.7	-2.4	-9.6	2.5	3.0	7.1	gmar
-77.722	19.841	-3.5	-23.1	-8.4	2.7	4.1	25.0	gcrz
-77.004	20.064	-3.6	-14.6	-0.2	4.3	6.2	23.1	glms
-75.851	20.186	-0.8	-1.0	-36.6	4.4	3.3	23.0	gslu
-76.363	20.358	1.0	-10.5	-27.5	3.3	3.8	27.4	gyar
-75.791	20.486	1.5	-4.6	-5.2	5.2	3.9	14.9	gpin
-76.749	18.004	13.9	-5.8	0.3	1.9	1.6	7.3	cn12
-77.652	18.491	30.3	-16.0	-4.3	2.5	2.1	9.4	falm
-77.606	17.905	25.5	-12.9	-19.9	1.8	1.5	6.8	junc
-76.788	17.975	15.8	-7.7	3.3	1.7	1.5	6.5	kngj
-77.031	18.138	21.4	-8.9	-7.0	2.0	1.7	7.9	lins
-77.242	17.808	18.2	-12.8	-10.5	1.9	1.7	7.3	lion
-78.172	18.446	42.7	-26.9	-12.2	1.8	1.6	7.0	luce
-76.894	18.370	17.0	-8.2	6.7	3.9	2.9	9.0	marj
-76.411	17.882	10.3	-5.3	-2.9	1.8	1.6	6.7	mora
-78.344	18.278	42.8	-26.9	-11.0	1.8	1.5	6.7	negr
-76.451	18.180	11.6	-4.7	0.4	1.9	1.6	7.5	prtj
-77.459	18.156	25.8	-11.7	-8.1	2.5	2.1	9.4	spau
-77.196	18.434	17.6	-10.5	-1.8	1.8	1.6	6.9	stan
-77.973	18.095	31.5	-18.5	-9.1	1.8	1.6	6.9	whtj
-77.352	18.306	30.0	-11.6	15.3	1.7	1.5	6.9	alex
-77.365	18.401	29.9	-14.5	26.6	3.6	3.3	21.5	btcc
-77.366	18.226	24.3	-8.3	-16.6	2.1	1.9	9.9	cave
-77.401	18.461	24.4	-14.5	-18.6	1.7	1.5	7.3	disc
-77.248	17.930	21.6	-21.1	20.2	1.9	1.6	8.2	hals
-77.452	18.150	27.0	-10.2	-14.1	2.1	1.9	9.0	knox
-77.499	18.014	27.8	-13.1	13.3	2.2	1.9	9.2	mand
-77.686	17.926	31.7	-12.7	40.4	2.0	1.7	8.6	mnro
-77.715	17.975	26.4	-14.4	-14.3	1.7	1.5	7.0	mvrn
-78.322	18.276	52.7	-22.5	-9.9	1.9	1.5	8.9	nglf
-77.157	17.742	21.4	-1.3	9.5	1.3	1.5	6.7	plnd
-77.137	17.749	25.2	-6.3	-5.4	1.6	1.4	6.7	warf

Table 1 List of the static coseismic offsets at the GPS sites used in the kinematic source inversion.

H (km)	Vp (km/s)	Poisson's ratio	Density (g/cm^3)
4.0	1.50	0.500	1.02
1.0	2.20	0.333	2.20
2.5	5.00	0.333	2.60
9.0	6.85	0.280	3.00

Table 2 Crustal velocity model at the source to compute seismograms at teleseismic distance.

H (km)	Vp (km/s)	Poisson's ratio	Density (g/cm^3)
30.0	6.00	0.250	2.70

Table 3 Crustal velocity model at the station to compute seismograms at teleseismic distance.

H (km)	Vp (km/s)	Poisson's ratio	Density (g/cm^3)
3.8	1.50	0.500	1.02
0.7	2.30	0.333	2.20
2.0	4.90	0.333	2.60
11.0	6.70	0.280	3.00

Table 4 Crustal velocity model at the source to compute the seismograms at teleseismic distance from the synthetic rupture model for the resolution test.

H (km)	Vp (km/s)	Poisson's ratio	Density (g/cm^3)
30.0	6.20	0.250	2.70

Table 5 Crustal velocity model at the station to compute the seismograms at teleseismic distance from the synthetic rupture model for the resolution test.

H	Vp	Vs	ρ	Qp	Qs
3.0	4.90	2.82	2.40	400.	200.
2.0	5.40	3.10	2.50	500.	250.
2.0	6.00	3.45	2.70	600.	300.
13.0	6.90	3.97	3.00	800.	400.
6.0	7.60	4.37	3.20	1000.	500.
8.0	7.80	4.48	3.30	1000.	500.
—	8.00	4.60	3.30	1000.	500.

Table 6 Velocity model derived from the study of Moreno et al. (2002) and used in this study to model the waveforms with the method of Bouchon (1981). H: layer thickness in km; Vp: P wave velocity in km/s; Vs: S wave velocity in km/s; ρ: density in g/cm^3 Qp and Qs: quality factor for the P and S waves respectively. Last layer with 0 thickness is the mantle half space.

H	Vp	Vs	ρ	Qp	Qs
5.0	4.90	2.83	2.5	500.	250.
5.0	6.20	3.58	2.7	600.	300.
14.0	6.80	3.93	3.0	800.	400.
—	8.10	4.68	3.3	1000.	500.

Table 7 Velocity model derived from the study of Moreno et al. (2002) and used in this study to model the waveforms with the method of Bouchon (1981) from the synthetic rupture model for the resolution test. H: layer thickness in km; Vp: P wave velocity in km/s; Vs: S wave velocity in km/s; ρ: density in g/cm^3; Qp and Qs: quality factor for the P and S waves respectively. Last layer with 0 thickness is the mantle half space.

Weight	Max. slip (m)	Average rupt. speed (km/s)	M_0 (N.m)
0.1	3.9	3.1	4.78×10^{20}
0.05	4.2	3.0	4.78×10^{20}
0.0	4.4	2.9	4.79×10^{20}

Table 8 Variation of maximum slip, average rupture speed and total seismic moment (M_0) when the weight of stations LCCY and FSCY is varied in the joint inversion of TELE, RBBSM and GPS data.

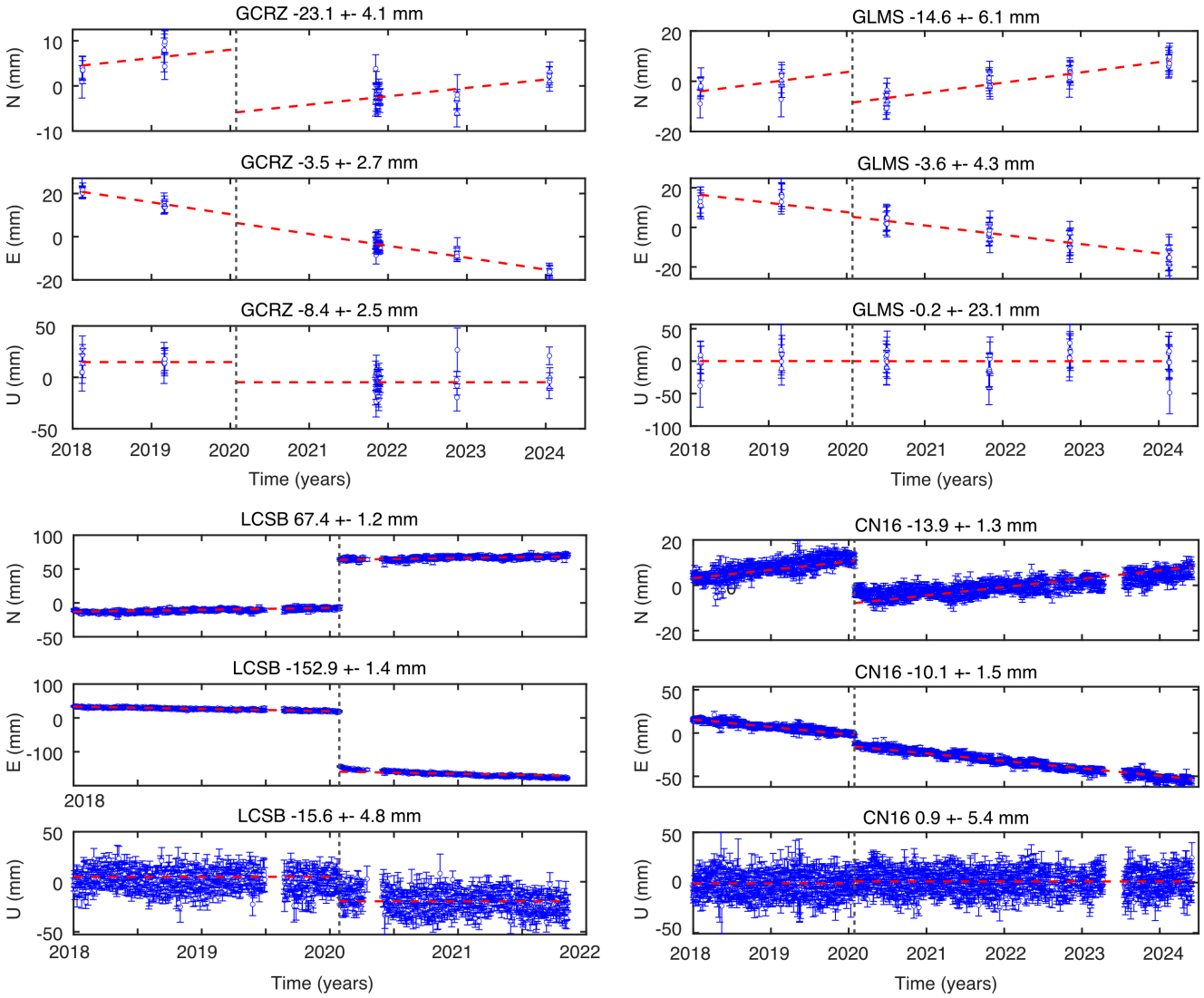

Figure 1 Position times series at four GPS stations. The top two are episodic, the bottom two continuous. Episodic stations GCRZ and GLMS are located in eastern Cuba, CN16 in central Cuba, and LCSB on the Cayman Islands. The vertical dashed line shows the time of the 28 January 2020, Mw7.7 Cayman Trough earthquake. Estimated coseismic displacements are given in mm above each panel. Note the short time interval of postseismic displacement visible at LCSB (east component) and CN16 (north component).

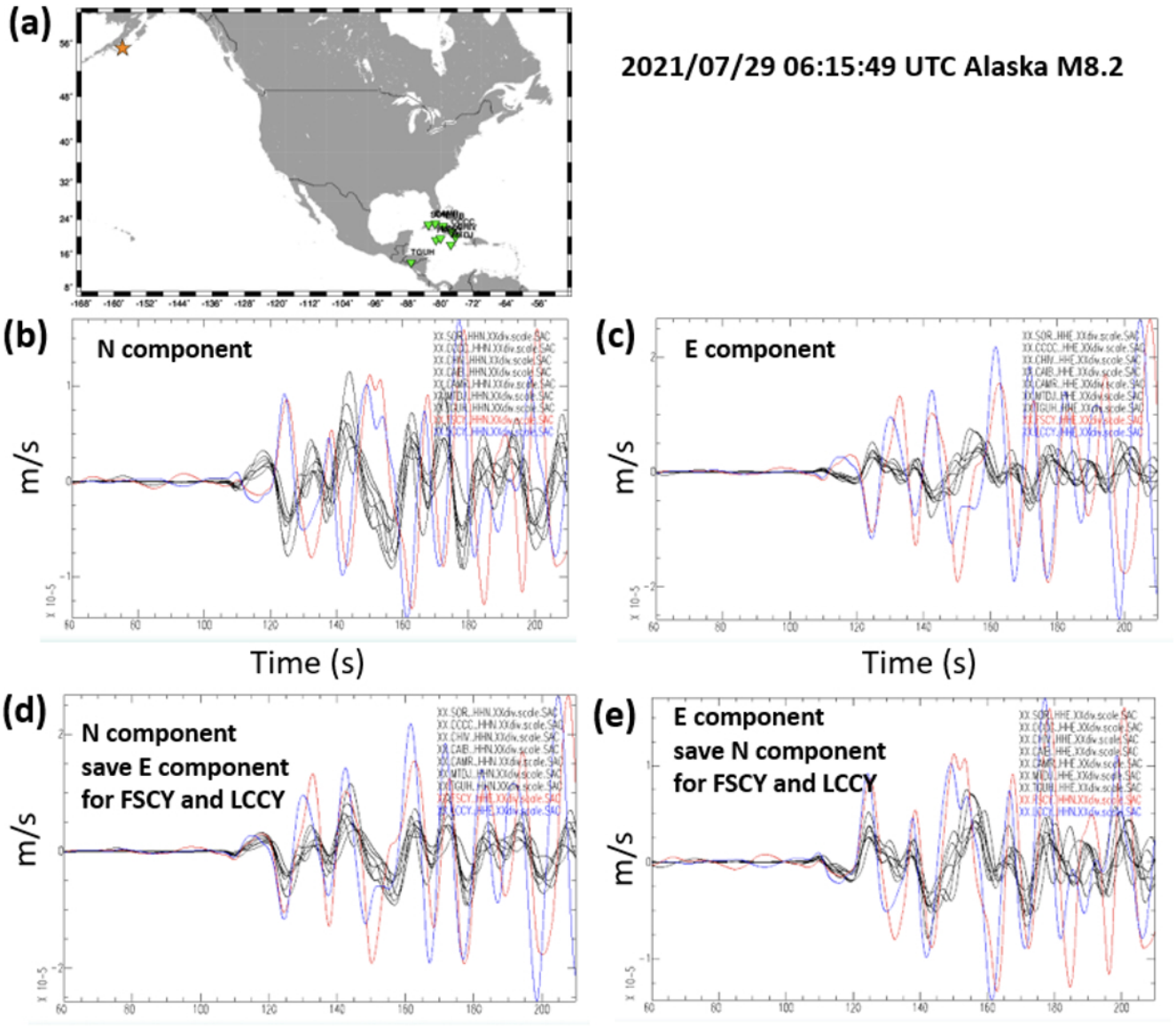

Figure 2 Comparison of broadband velocity records at stations in the Caribbean and Middle America for a teleseismic event of M8.2 in Alaska in 2021. All signals are divided by the sensibility of their respective station, and band-passed between 0.03 and 0.1 Hz. (a) Map showing the epicenter (orange star) and the stations (SOR, CCCC, CHIV, CAIB, CAMR, MTDJ, TGUH, FSCY, LCCY, green triangles). (b) Superimposed plots of the North component of all stations. Traces in black, save FSCY in red and LCCY in blue. Note that FSCY and LCCY have opposite phase with respect to the other stations. (c) Superimposed plots of the East component of all stations. Traces in black, save FSCY in red and LCCY in blue. Note that FSCY and LCCY have opposite phase with respect to the the other stations. (d) Superimposed plots of the North component of all stations, save FSCY and LCCY for which the East component is plotted. Traces in black, save FSCY in red and LCCY in blue. Note that FSCY and LCCY are now in phase with the other stations, but with amplitudes about twice larger. (e) Superimposed plots of the East component of all stations, save FSCY and LCCY for which the North component is plotted. Traces in black, save FSCY in red and LCCY in blue. Note that FSCY and LCCY are now in phase with the other stations, but with amplitudes about twice larger. This indicates that the original N and E components of stations FSCY and LCCY are exchanged, with a sensitivity value about twice too small.

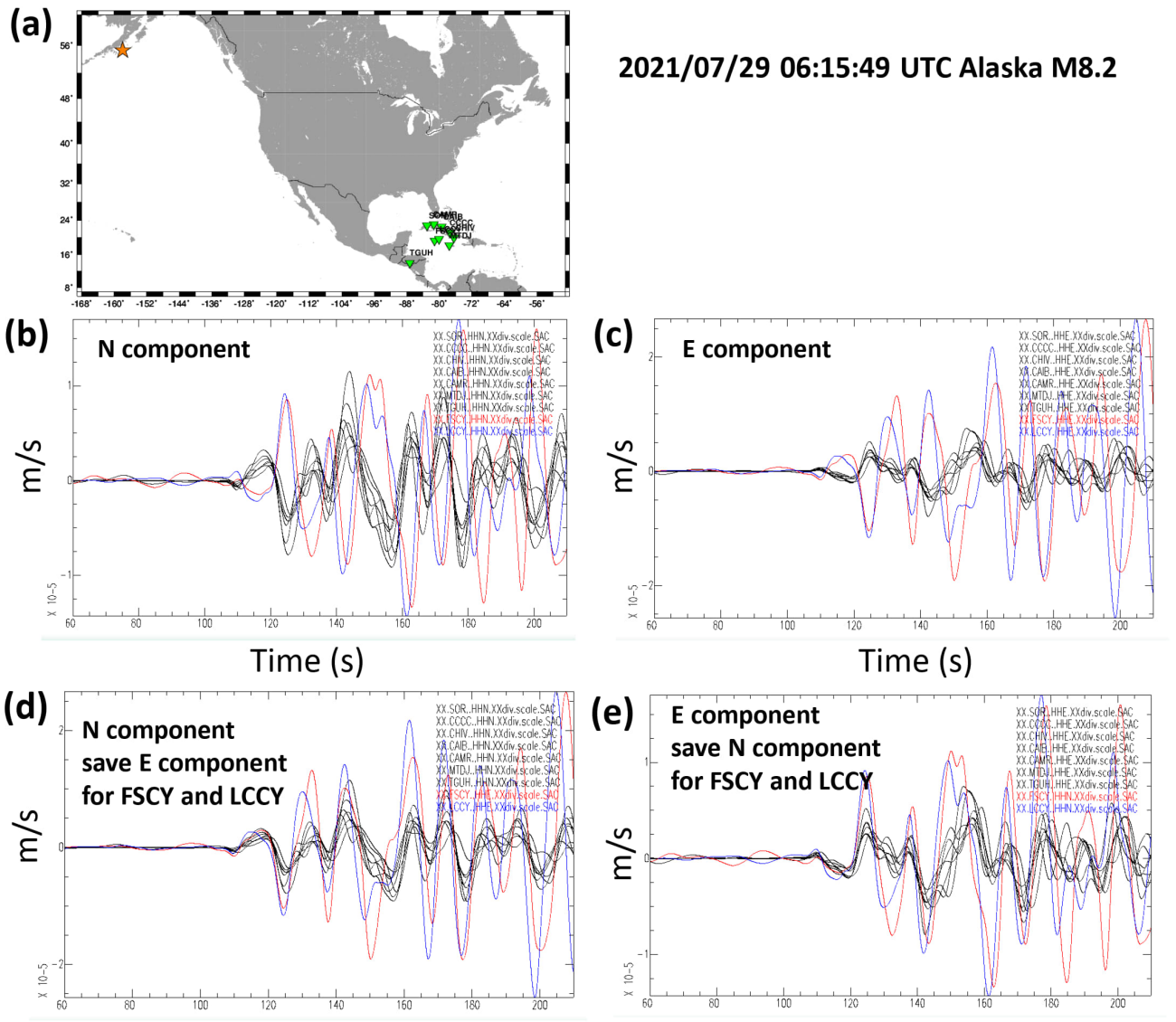

Figure 3 Comparison of GPS coseismic static displacements at station LCSB with the static displacement estimated from the strong motion records at the collocated station LCCY. (a) Map showing the location of stations LCSB and LCCY (yellow triangle), the coseismic displacement vector, and the measured values of the north and east coseismic offsets. Also shown, the trace of the fault model (thin straight line, and the mainshock epicenter (small orange star). (b) Careful double integration of the strong motion record of the east component of station LCCY (channel HNE), divided by the sensibility of the station, converted into cm, and finally divided by a factor of 2. We observe that the displacement record stabilizes around a constant value of about +7.5 cm, interpreted as the static offset. The static offset thus estimated is similar to the north offset of +7 cm at the collocated GPS station LCSB. (c) Careful double integration of the strong motion record of the north component of station LCCY (channel HNN), divided by the sensibility of the station, converted into cm, and finally divided by a factor of 2. We observe that the displacement record stabilizes around a constant value of about -15.3 cm, interpreted as the static offset. The static offset thus estimated is similar to the east offset of -15 cm at the collocated GPS station LCSB. This confirms that the original N and E components of stations LCCY are exchanged, with a sensitivity value about twice too small.

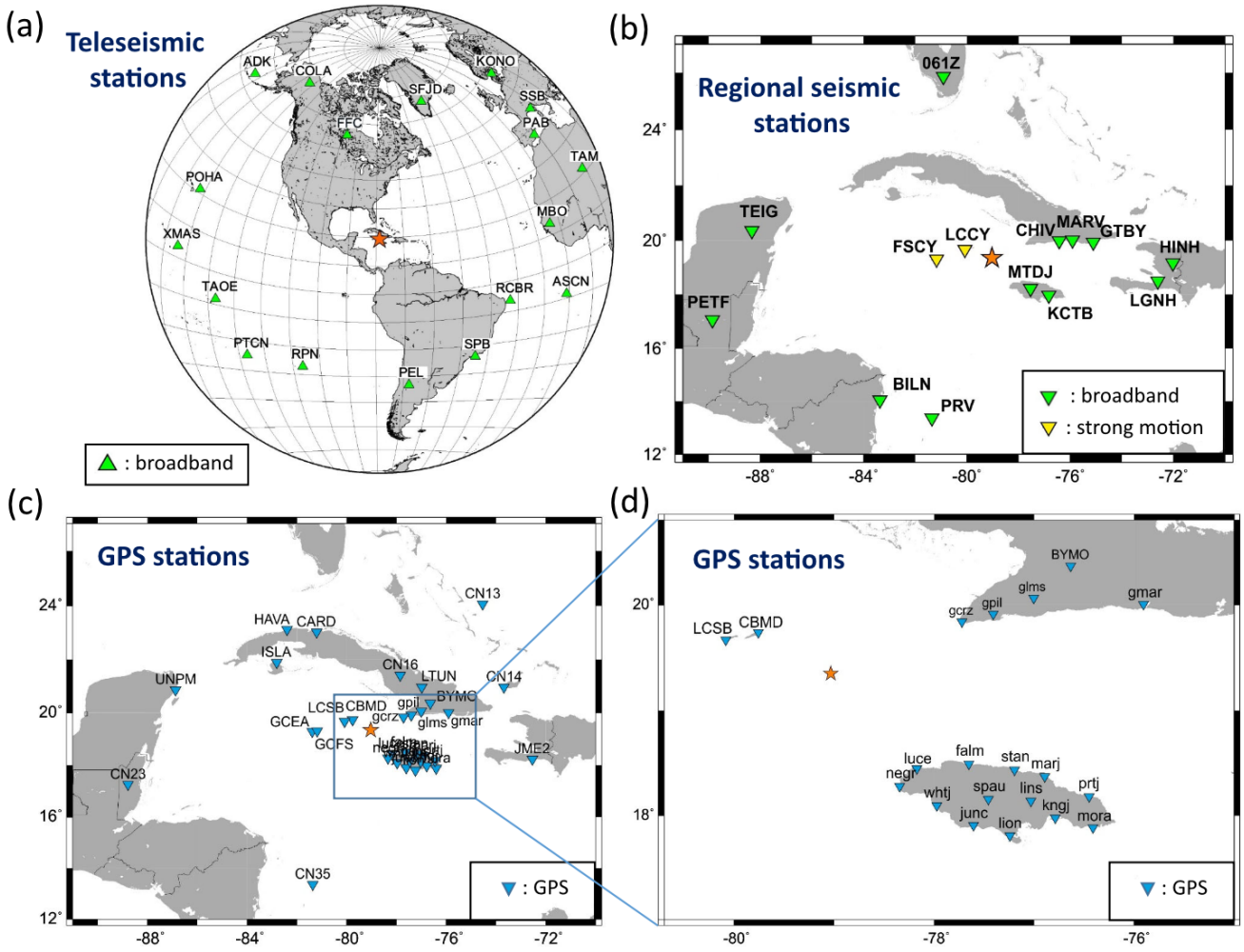

Figure 4 Seismic and GPS stations used in the kinematic inversion. The orange star is the mainshock epicenter from this study. (a) Teleseismic broadband stations (TELE). (b) Regional broadband and strong motion stations (RBBSM). (c) and (d) GPS stations.

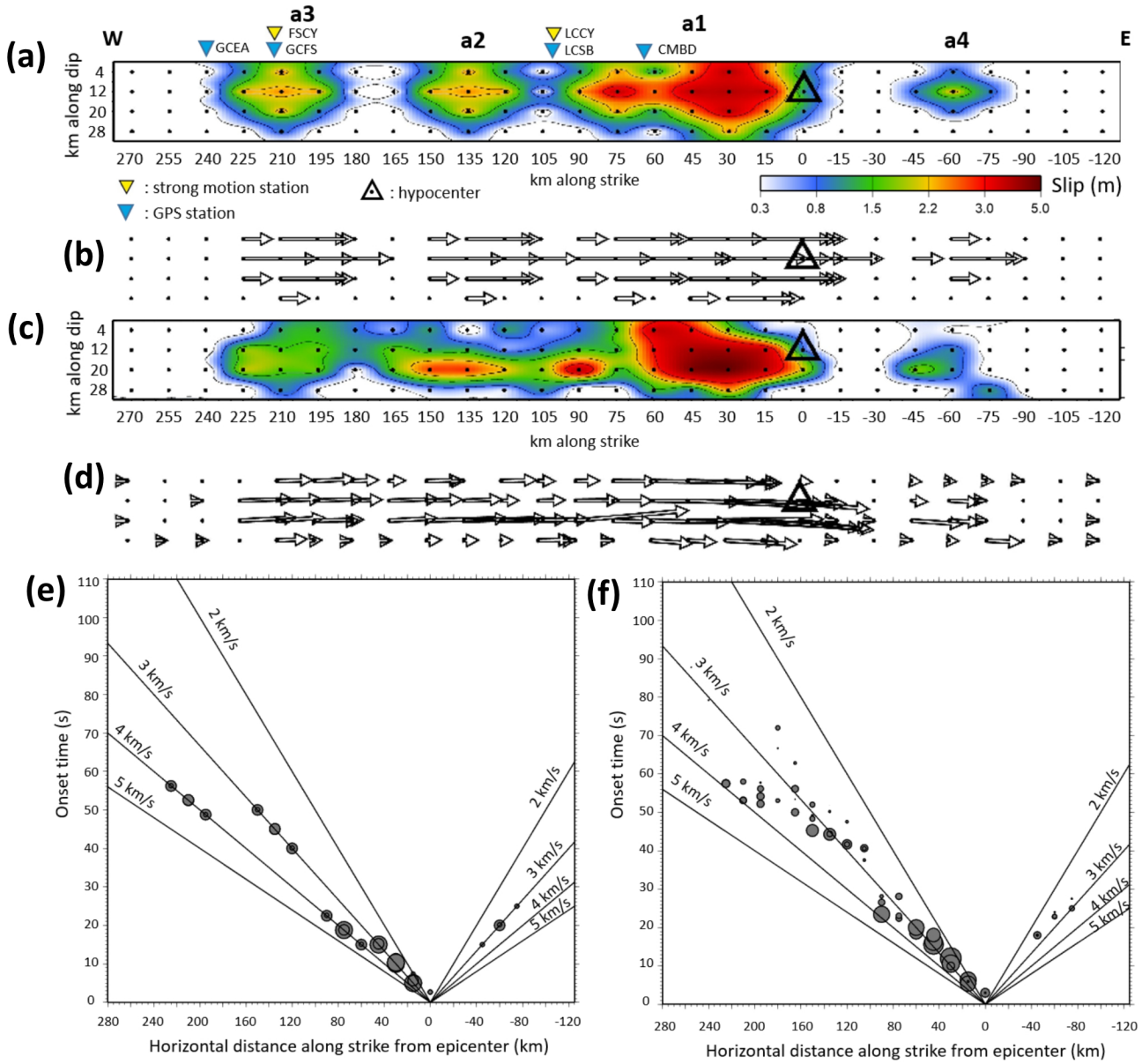

Figure 5 Test of the spatial and temporal resolution of the slip distribution kinematic inversion. (a) and (b): synthetic slip and rake distribution with main slip areas are labeled a1 to a4, used to compute synthetic observations at the TELE, RBBSM, and GPS stations. (c) and (d): slip and rake distribution from the joint inversion of synthetic data at the TELE, RBBSM and GPS stations. (e): rupture timing of the synthetic model. (f): rupture timing recovered by the joint inversion of synthetic data at the TELE, RBBSM and GPS stations. There are fewer circles in the synthetic model (panel e) than in the inversion (panel f) because some sub-faults in the input synthetic model are at rest, with zero slip, but are slipping in the inverted model. Also, some circles are superimposed on the synthetic model graph because they occur about at the same epicentral distance. See also captions of Figures 4 and 5.

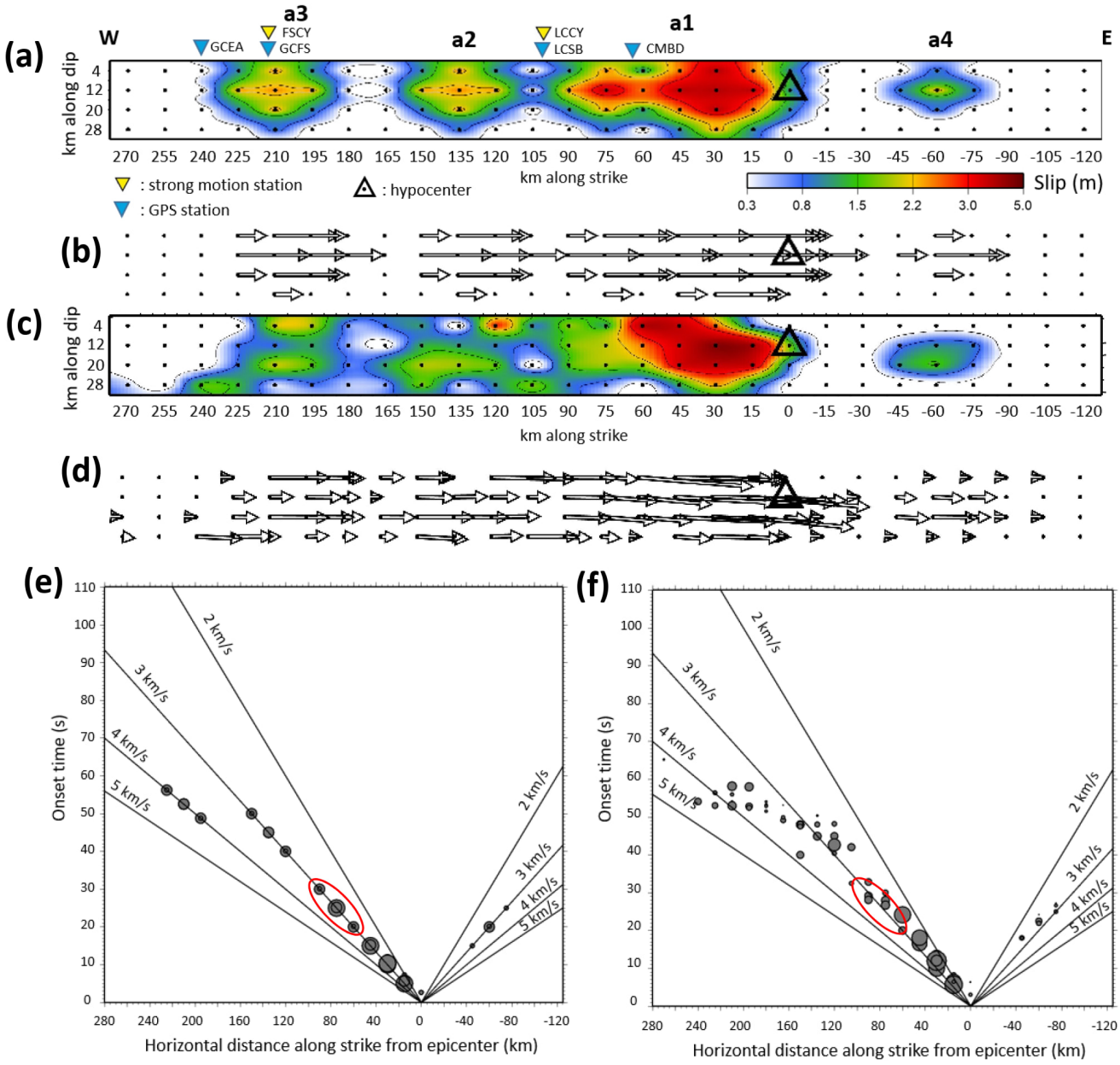

Figure 6 The caption is the same as for Figure 5, but here the input synthetic model is slightly different. The westernmost patch of slip area a1 (epicentral distance between 60 and 90 km), corresponding to segment FLVR1 in the manuscript, ruptures at subshear velocity (3 km/s). The segment is indicated by the surrounding red ellipse in panels (e) (synthetic model) and (f) (inverted model).

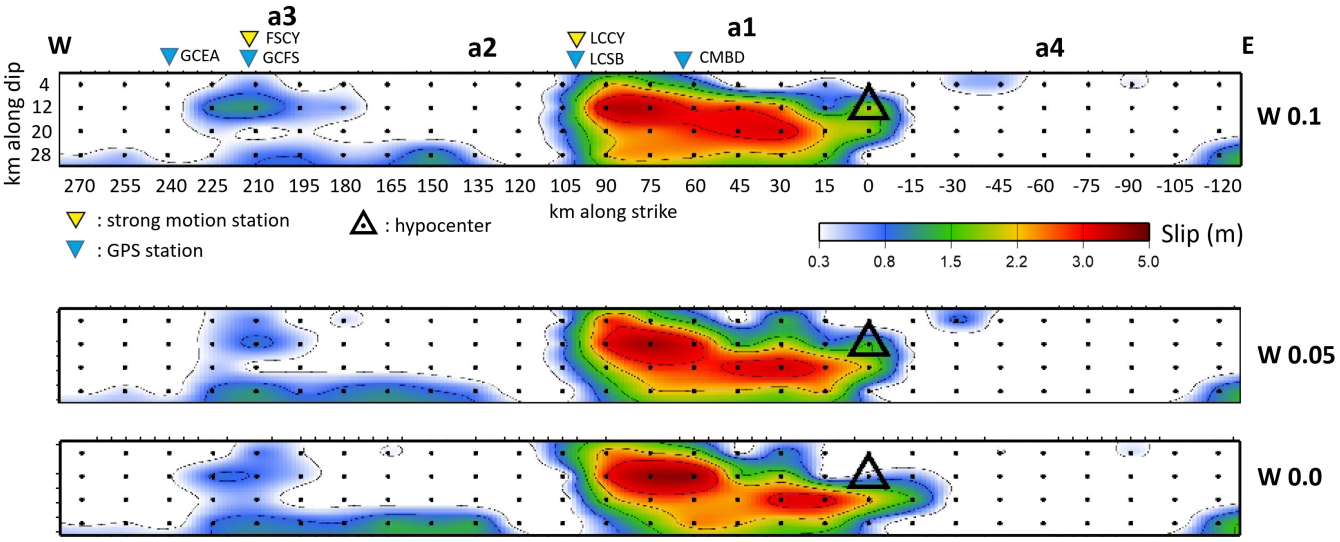

Figure 7 Slip distribution from the joint inversion of TELE, RBBSM, and GPS data with variable weights (W) for stations FSCY and LCCY. Small black dots represent the grid of point sources along the fault model. The top panel shows results for a weight of 0.1, the middle panel for a weight of 0.05, and the bottom panel for a weight of zero.

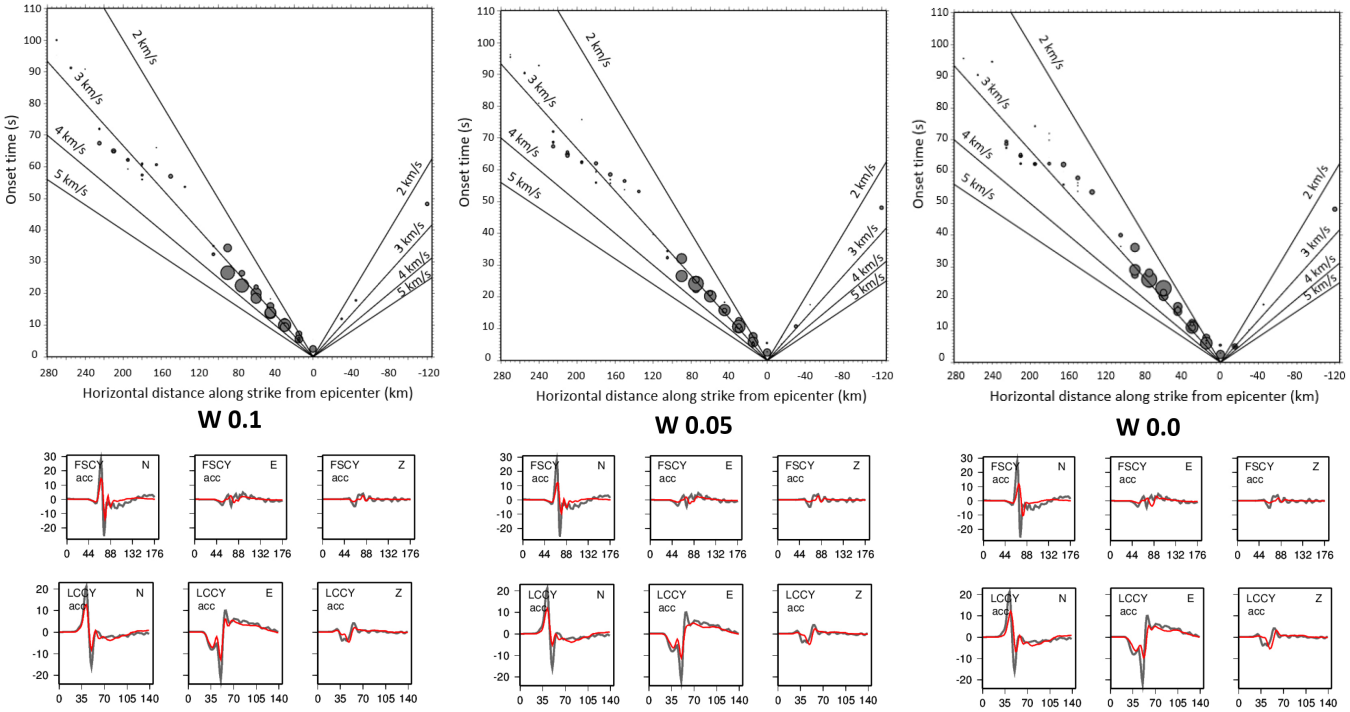

Figure 8 Rupture timing (top) and waveform fit of stations FSCY and LCCY (bottom) from the joint inversion of TELE, RBBSM, and GPS data with variable weights (W) for stations FSCY and LCCY. The left panel shows results for a weight of 0.1, the middle panel for a weight of 0.05, and the right panel for a weight of zero. The captions for rupture timing and waveform fit are the same as in previous figures.

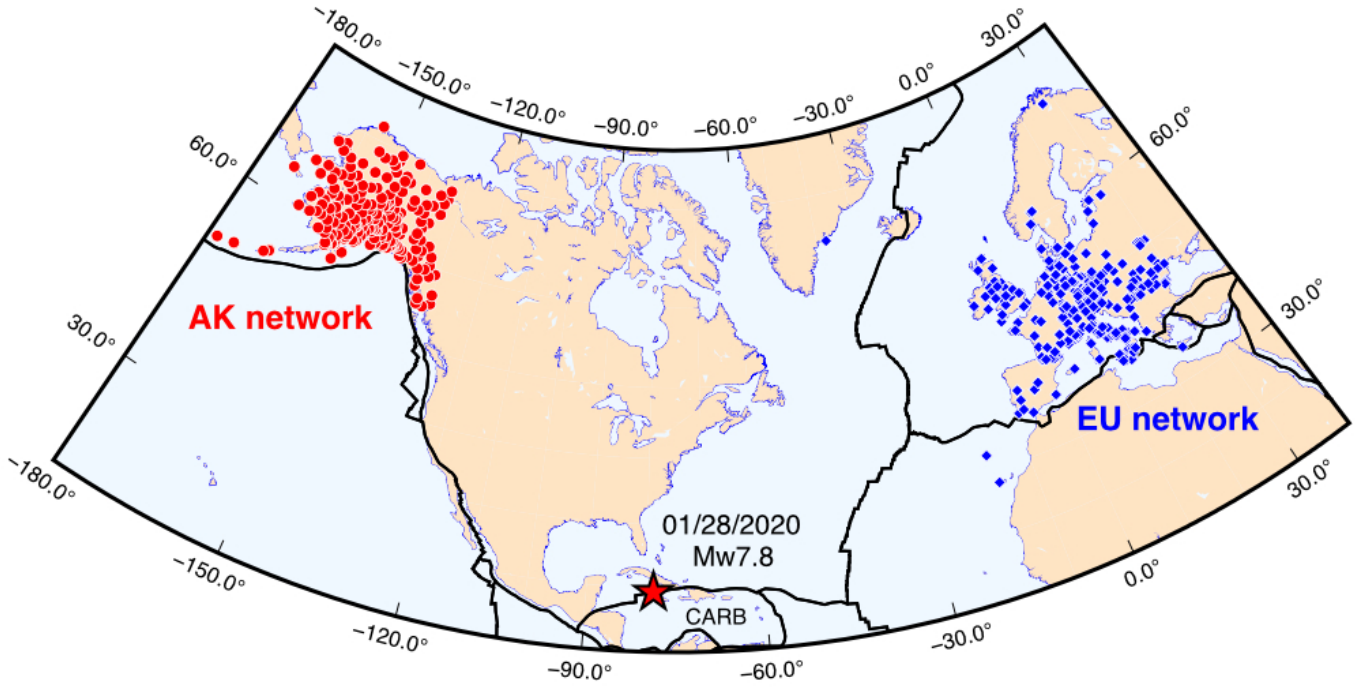

Figure 9 Map of the broadband seismic networks used in the back-projection analysis, with 211 stations from the Alaska network (AK) and 301 stations from the European network (EU). Black lines show plate boundaries. The Caribbean plate is labeled "CARB". The red star is the epicenter of the 28 January 2020, Mw7.7 earthquake on the Oriente transform fault.